Journal of Engineering Mathematics (2006) 55: 65–80
DOI 10.1007/s10665-005-9006-1

Numerical investigation of three-dimensional bubble dynamics

K.E. AFANASIEV and I.V. GRIGORIEVA
Kemerovo State University, Kemerovo, Krasnay st. 6, Russia (E-mails: afa@kemsu.ru, irene@kemsu.ru)

Received 22 December 2003; accepted in revised form 30 June 2005 / Published online: 15 November 2005

Abstract. This work is devoted to a numerical investigation of three-dimensional gas-vapor bubble dynamics. Bubble oscillations in ambient unbounded fluid and interaction of the bubble with different inclined solid walls are investigated numerically. The fluid is assumed inviscid and incompressible and the flow is irrotational. The boundary-integral method is used as an instrument of numerical investigation. Much attention is paid to the description of a numerical algorithm. Its conservative character is verified by control over conservation of energy. Certain characteristics of the impact jet, which often emerges during the bubble-collapse phase, are investigated numerically. These are the jet height and the direction and velocity of the jet peak. The jet-penetration coefficient is described to estimate the erosion effect on the wall. Dimensional values for different types of bubbles, cavitation bubbles and bubbles formed as a result of different charge explosions are determined.

Key words: bubble, bubble oscillation, cumulative effect, impact jet

1. Introduction

This work is devoted to a numerical investigation of three-dimensional gas-vapor bubble dynamics. Bubble oscillations in ambient unbounded fluid and interaction of the bubble with different inclined solid walls are investigated. The fluid is assumed inviscid and incompressible and the flow is irrotational. As an instrument of numerical investigation we use the boundary-integral method, the third Green formula being invoked as its basic relation.

The model described in this work is applied to simulate seemingly different phenomena. On the one hand, the dynamics of underwater explosions is considered, on the other, the dynamics of a single cavitation bubble is studied. The applicability of this model for investigating these effects is discussed [1, pp. 301–308], [2]. What do these seemingly different phenomena have in common? One such feature is the arising reentrant jet. A bubble, developed from a tiny cavity (if it is a cavitation bubble), or formed during the explosion of a charge (if an underwater explosion is considered), as a rule, keeps its shape close to spherical during the process of its growth. At its maximum volume, the bubble turns into the collapse phase. In case of the absence of factors braking the bubble's spherical symmetry, one can observe the phenomenon of bubble oscillations. When the growth phase and the collapse phase alternate repeatedly, bubble evolution acquires an oscillating character. Proximity to a solid boundary and (or) gravity disturb the one-dimensional character of the flow, even if at the moment of maximum volume the bubble was spherical. Sometimes a jet of fluid is formed during the bubble-collapse process and introduced into the bubble up to the moment when the opposite wall is touched. This jet may be directed toward the wall and have a velocity of several hundred or, under certain conditions, even thousands of meters per second. If the jet is directed toward the wall, particles on the bubble surface most distant from the wall get a larger acceleration, *i.e.*, the classical cumulative effect takes place. The assumption, that the target destruction mechanism is determined only by the influence of a high-speed reentrant

jet, formed during the bubble-collapse stage, has proved unjustified in the axisymmetric formulation, when the gravity and Bjerknes forces act along the axis of symmetry in one or opposite directions [3]. Therefore, the actual problem is to determine different characteristics of the jet, such as its direction, velocity, height and the direction of its development for the analysis of the erosive effect in the 3d case. This work also describes a method for estimating the damage to the solid wall caused by the bubble as well as determining dimensional values for different types of bubbles.

The problem of bubble dynamics has long been an important research field. Both theoretical and experimental approaches have been applied to investigate this problem; and finally the preferred approach has become a numerical experiment. In this respect we should first of all mention the innovative work of Benjamin and Ellis [4]. The history of investigation of this problem is described quite exhaustively in [5]. We should also mention some work by representatives of the Russian scientific school, *e.g.* [1], [6], [7, Chapter 2]. This work pays special attention to a description of the numerical algorithm. At present, numerical investigation of three-dimensional problems is already quite advanced owing to modern computing capabilities and, moreover, is not out of the ordinary. However, analysis of the results is still a difficult and laborious process. In this connection, the number of works devoted to the investigation of three-dimensional bubble motion and deformation is still small and insufficient. In this respect, we should mention the excellent work by Blake *et al.* [8], Wang [5], Xi *et al.* [9] and Wang [10]. (The latter paper was published after our paper had been submitted). A number of authors have succeeded in simulating the transition from a cavitating bubble to a torus in the axisymmetric formulation; see, for example, [11,12]. In these works, as in the present work, the authors apply the boundary-integral method based on the third Green formula for investigations of three-dimensional bubble (or several bubbles) motion. Due to the complexity of this problem, methods applied for its solution also vary considerably. Application of the finite-element method to problems of bubble evolution is described in [13,14], of the volume-of-fluid method in [15], of the Langrange-Thomson method in [16] and the generalized vortex method in [17]. Since the present work was started rather long ago [18,19], the numerical algorithm has been thoroughly investigated; different boundary-mesh-construction methods, integral coefficient calculations, methods for solving linear algebraic equation systems have been tried and methods for calculating the velocity field have been developed. The method of time coordinate motion has been taken from the axisymmetric problem implementation [20], and turned out to be very effective. The conservative nature of the numerical algorithm can be tracked by controlling the conservation of energy.

2. Theory

Let us consider a transient fluid area $\Omega(t)$ bounded by surfaces, namely, S – inclined wall, $\Gamma(t)$ – bubble surface and $Q(t)$ being the bubble area (Figure 1). The fluid is assumed inviscid and incompressible and the flow is irrotational. The pressure inside the bubble is the sum of the saturated vapor pressure p_v and the pressure of the gas which, as we will assume, follows the adiabatic law $p_g = p_0(V_0/V(t))^{\lambda}$, where $V(t)$ is the bubble volume, p_0, V_0 are the initial gas pressure and bubble volume and λ is the ratio of specific heats. In this work we take $\lambda = 1{\cdot}4$. We neglect gas diffusion through the bubble boundary, *i.e.*, the pressure on the bubble boundary $\Gamma(t)$ is defined as $p_\Gamma = p_v + p_g$.

At the initial moment of time the bubble is a sphere S_0 with radius R_0. It is known from experimental data that the bubble maintains its shape close to spherical for most of its lifetime. There is a mathematical problem description for the velocity potential φ in nondimensional

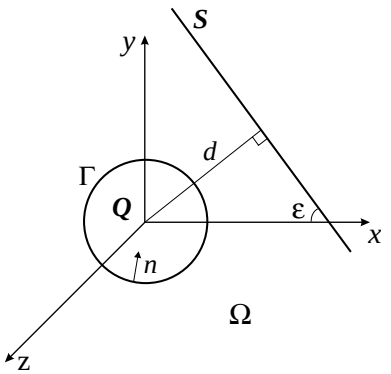

Figure 1. Location of the bubble and the wall in a Cartesian coordinate system.

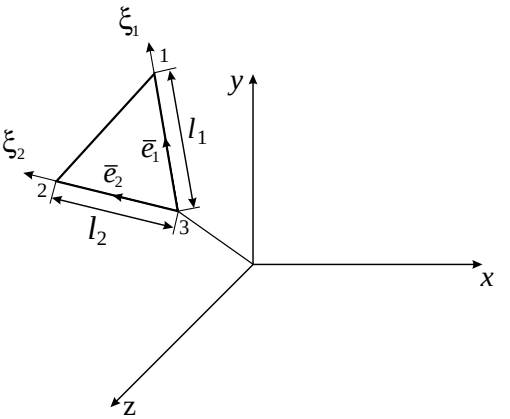

Figure 2. Local coordinate system on the triangular element.

variables. The velocity potential satisfies Laplace's equation

$$\Delta\varphi = 0, \qquad x \in \Omega(t) \tag{1}$$

and the kinematic and dynamic boundary conditions:

$$\frac{\mathrm{d}x}{\mathrm{d}t} = \nabla\varphi, \qquad x \in \Gamma(t), \tag{2}$$

$$\frac{\mathrm{d}\varphi}{\mathrm{d}t} = 1 + \frac{1}{2}|\nabla\varphi|^2 - \alpha z - \beta\left(\frac{V_0}{V}\right)^{\lambda}, \quad x \in \Gamma(t), \tag{3}$$

The parameters are scaled with respect to R_m for lengths, where R_m is the maximum radius that the vapour bubble would attain in an infinite fluid domain at a uniform pressure of p_∞, $R_m\sqrt{\rho/\Delta p}$ for time, where $\Delta p = p_\infty - p_v$ and ρ is the liquid density, $\sqrt{\Delta p/\rho}$ for velocity and $R_m\sqrt{\Delta p/\rho}$ for the potential, $\alpha = R_m\rho g/\Delta p$ is the buoyancy coefficient, g denotes the gravity acceleration and $\beta = p_0/\Delta p$ describes the initial gas pressure in the bubble.

On the solid boundary the potential satisfies the impermeability condition

$$(\nabla\varphi, \overline{n}) = 0, \quad x \in S. \tag{4}$$

The problem (1–4) is supplemented by the condition that the fluid is quiescent at infinity (5).

$$|\nabla\varphi| \to 0, \qquad |\overline{x}| \to \infty. \tag{5}$$

Further, it is necessary to specify the free-boundary location at the initial moment of time $t = 0$ and the potential distribution on it:

$$\Gamma|_{t=0} = \Gamma_0, \qquad \varphi|_{t=0} = \varphi(0, \bar{x}). \tag{6}$$

Therefore, the boundary-value problem of the gas-vapor bubble evolution is described by Equation (1) with boundary conditions (2–5) and initial conditions (6). The problem statement is traditional for these kinds of flow. The problem is nonlinear because of the nonlinearity of the dynamical condition and the unknown location of the bubble boundary for $t > 0$. We seek to calculate the fluid motion and the location of the bubble surface $\Gamma(t)$ for $t > 0$.

3. Numerical simulation

The nonlinear boundary-value problem (1–6) may be reduced to a sequence of linear problems at each time step. To achieve that, one must execute a transition to a finite-difference approximation of time derivatives with the variable step Δt_j in the boundary conditions (2, 3), where j denotes the number of the time step. The time step is selected automatically and based on the condition that the mesh points can not be moved further than the prescribed distance

$$\Delta t \leq \frac{\zeta l^j_{\min}}{\max_i |\Delta\varphi(\bar{x_i}, t)|},$$

where i is the mesh-node number, $l^j_{\min}$ the minimum lengths of the mesh edge and ζ the empirical coefficient which should be selected so that the estimated time of bubble collapse coincides with the well-known analytical solution of the Rayleigh problem [7]. The time step depends directly on the kind of mesh approximating the bubble surface, and on the velocity of its motion. For example, for a mesh consisting of 602 nodes and 1200 elements, we have $\zeta = 0{\cdot}0102$, and for a mesh consisting of 642 nodes and 1280 elements we have $\zeta = 0{\cdot}0168$. The method of mesh generation is described below. A similar method regarding the time-coordinate motion is described in [21]. Naturally, there are values $\Delta t_{\min}$ and $\Delta t_{\max}$ which limit the maximum and minimum time step: in our case $\Delta t_{\min} = 0{\cdot}0001$ and $\Delta t_{\max} = 0{\cdot}01$.

To solve the problem (1) with the boundary conditions (4) and (5) we apply a boundary-element method, the third Green formula being invoked as its basic relation

$$C(x)\varphi(x) + \int_\Gamma \varphi(x,\xi)q^*(x,\xi)\mathrm{d}\Gamma(\xi) = \int_\Gamma q(x,\xi)\varphi^*(x,\xi)\mathrm{d}\Gamma(\xi), \tag{7}$$

where $q = \partial\varphi/\partial n$ and φ^* is the fundamental solution of the Laplace equation, which is written in the spatial case as $\varphi^*(\bar{x},\bar{\xi}) = \frac{1}{4\pi|\bar{x}-\bar{\xi}|}$; here $\bar{x}$ is the collocation point and ξ – current point on the boundary Γ; $q^* = \partial\varphi^*/\partial n$. In the case of bubble evolution near a flat solid wall under consideration, the Green function consists of the source located in the point ξ and of the source in the point ξ', positioned symmetrically to ξ with respect to the boundary Γ: $\varphi^*(\bar{x},\bar{\xi}) = \frac{1}{4\pi}\left(\frac{1}{|\bar{x}-\bar{\xi}|} + \frac{1}{|\bar{x}-\bar{\xi}'|}\right)$. Hence, the impermeability condition on the solid boundary (4) is fulfilled automatically, which allows reducing essentially the calculation volume required for the problem solution. For bubble evolution near an L-shaped solid wall, one can also write down the Green function giving automatic fulfillment of the impermeable condition

$$\varphi^*(\bar{x},\bar{\xi}) = \frac{1}{4\pi}\left(\frac{1}{|\bar{x}-\bar{\xi}|} + \frac{1}{|\bar{x}-\bar{\xi}'|} + \frac{1}{|\bar{x}-\bar{\xi}''|} + \frac{1}{|\bar{\xi}'-\bar{\xi}''|}\right),$$

where $\bar{\xi}'$ is the point symmetrical to $\bar{\xi}$ with respect to one of the walls, forming the angle and $\bar{\xi}''$ with respect to the other. The coefficient $C(\bar{x}) = \omega/2\pi$, where ω is a solid angle at which the surface is seen from the point $\bar{x}$.

The bubble surface Γ is approximated by a set of plane triangular elements. Let us consider two different approaches to building a surface boundary-element mesh. In the first approach the initial surface is divided into separate triangular supporting zones. Each of the supporting zones imaged into the canonical domain is divided into a prescribed number of elements. Backward transformation allows forming the required surface mesh [22]. The number of mesh nodes N and elements M are determined by the number of zones and by partition of each separate zone. While the first approach is universal, the second is suited specifically for building a mesh on

the surface of a sphere. The initial approximation of the sphere for the second algorithm is an icosahedron, each edge of which is bisected by a new mesh node. The obtained nodes are moved onto the surface of the sphere and combined into a new element. At each new discretization level, each element of the preceding level is transformed into four new elements. In this case, the number of mesh nodes and elements increases very rapidly, *viz.* $N = 5 \times 2^{2n-1} + 2$, $M = 5 \times 2^{2n}$, where n denotes the level of discretization; hence, we obtain only one acceptable computational mesh consisting of 642 nodes and 1280 elements. The advantage of the second approach is that the mesh, built by means of it, is more uniform; thus, in the first case, the ratio of the largest square of an element to its smallest square tends to 1·85, in the second case to 1·3. However, using the more regular mesh does not provide any noticeable advantage, even for calculations with sufficient deformation of the bubble boundary.

Let us suppose the functions φ and q are linear functions on the elements. A local system of coordinates is introduced on the elements (Figure 2); then $\bar{r} = x_3\bar{i} + y_3\bar{j} + z_3\bar{k} + l_1\xi_1\bar{e_1} + l_2\xi_2\bar{e_2}$, where l_1, l_2 are the lengths of the element sides, and $\bar{e_1}, \bar{e_2}$ denote unit base vectors of the introduced coordinates system with ξ_1, ξ_2 varying along the element side from 0 to 1 and $\xi_3 = 1 - \xi_1 - \xi_2$. The integral coefficients of the boundary-integral method are written as follows

$$h_{ij}^k = -\frac{S_j}{2\pi}\int_0^1\int_0^{1-\xi_2} \xi_k \frac{\cos\alpha(x-x_i) + \cos\beta(y-y_i) + \cos\gamma(z-z_i)}{|\bar{x}-\bar{x_i}|^3}\mathrm{d}\xi_1\mathrm{d}\xi_2$$

$$= -\frac{S_j}{2\pi}\int_0^1\int_0^{1-\xi_2} \xi_k \frac{a_7\xi_1 + a_8\xi_2 + a_9}{(a_1\xi_1^2 + a_2\xi_2^2 + a_3\xi_1\xi_2 + a_4\xi_1 + a_5\xi_2 + a_6)^{3/2}}\mathrm{d}\xi_1\mathrm{d}\xi_2$$

$$g_{ij}^k = \frac{S_j}{2\pi}\int_0^1\int_0^{1-\xi_2} \frac{\xi_k}{|\bar{x}-\bar{x_i}|}\mathrm{d}\xi_1\mathrm{d}\xi_2 =$$

$$= \frac{S_j}{2\pi}\int_0^1\int_0^{1-\xi_2} \frac{\xi_k}{(a_1\xi_1^2 + a_2\xi_2^2 + a_3\xi_1\xi_2 + a_4\xi_1 + a_5\xi_2 + a_6)^{1/2}}\mathrm{d}\xi_1\mathrm{d}\xi_2.$$

Here i is the number of collocation points with $i = \overline{1, N}$, j denotes the element number with $j = \overline{1, M}$, S_j is the j-th element square, $k = \overline{1, 3}$ the local node number on the element and $\bar{n} = (\cos\alpha, \cos\beta, \cos\gamma)$ denotes the normal vector for the j-th element. The coefficients a_m are defined as follows:

$$a_1 = |\bar{x_1} - \bar{x_3}|^2, \quad a_2 = |\bar{x_2} - \bar{x_3}|^2, \quad a_3 = 2(\bar{x_1} - \bar{x_3})(\bar{x_2} - \bar{x_3}),$$

$$a_4 = 2(\bar{x_1} - \bar{x_3})(\bar{x_3} - \bar{x_i}), \quad a_5 = 2(\bar{x_2} - \bar{x_3})(\bar{x_3} - \bar{x_i}), \quad a_6 = |\bar{x_3} - \bar{x_i}|^2,$$

$$a_7 = (\bar{x_1} - \bar{x_3})\bar{n}, \quad a_8 = (\bar{x_2} - \bar{x_3})\bar{n}, \quad a_9 = (\bar{x_3} - \bar{x_i})\bar{n},$$

$$a_{10} = 2(\bar{x_1} - \bar{x_3})(\bar{x_1} - \bar{x_i}), \quad a_{11} = 2(\bar{x_1} - \bar{x_3})(\bar{x_2} - \bar{x_i}),$$

$$a_{12} = 2(\bar{x_2} - \bar{x_3})(\bar{x_1} - \bar{x_2}), \quad a_{13} = |\bar{x_1} - \bar{x_i}|^2,$$

$$a_{14} = 2(\bar{x_2} - \bar{x_1})(\bar{x_1} - \bar{x_i}), \quad a_{15} = |\bar{x_1} - \bar{x_2}|^2.$$

When x_i does not belong to the element Γ_j, the integrals h_{ij}^k and g_{ij}^k are regular; in this case the inner integrals are calculated analytically, whereupon the obtained integrals are calculated by Gaussian quadrature at seven points. As an example let us write down the expression for the integral g_{ij}^1:

$$g_{ij}^1 = \frac{S_j}{2\pi\sqrt{a_1}} \int_0^1 \xi_1 \log\left(\frac{a_{10} + a_{11}\xi_1 + 2\sqrt{a_1}\sqrt{a_{13} + a_{14}\xi_1 + a_{15}\xi_1^2}}{a_4 + a_3\xi_1 + 2\sqrt{a_1}\sqrt{a_6 + a_5\xi_1 + a_2\xi_1^2}} \right) \mathrm{d}\xi_1$$

When the node x_i coincides with one of the vertices of the element Γ_j, the integrals h_{ij}^k and g_{ij}^k have a singularity. The integrals h_{ij}^k have a strong singularity $(1/|x - x_i|^3)$, but make zero contribution to the resulting system of equations, since the kernel numerator is a scalar product of the vector lying in the element plane and its orthogonal vector $\bar{n}$. The integrals g_{ij}^k have a singularity of the $(1/|x - x_i|)$ kind; in this case the inner integrals are calculated analytically, whereupon the indefinite expressions are calculated according to the l'Hospital rule and the obtained integrals are also calculated by seven-point Gaussian quadrature. The singular integral g_{ii}^1 in turn is obtained as follows:

$$g_{ii}^1 = \frac{S_j}{2\pi\sqrt{a_2}} \int_{-1}^1 \xi_2 \log(2a_2 + a_{12}\xi_2 + 2\sqrt{a_2}\sqrt{a_2 + a_{12}\xi_2 + a_{15}\xi_2^2})\mathrm{d}\xi_2 - \frac{S_j}{2\pi\sqrt{a_2}} \left(\frac{1}{2} \log(2\sqrt{a_1 a_2} + a_3) + \frac{1}{4} \right).$$

We obtain the coefficients H_{ij} and G_{ij} by adding h_{ij}^k and g_{ij}^k to the corresponding values of the potential and normal derivative for all collocation points. The coefficients C_i can be determined from the following considerations. If the constant potential $\varphi = \text{const}$ is defined on the boundary, the flow through the boundary equals zero and $C_i = -\int_\Gamma q^*(\bar{x}, \bar{\xi})\mathrm{d}\Gamma(\bar{\xi})$ for bounded domains, and $C_i = -\int_\Gamma q^*(\bar{x}, \bar{\xi})\mathrm{d}\Gamma(\bar{\xi}) + 1$ for domains with an infinite boundary. In this way the computational cost for determining the spatial angles is negligible since; to calculate C_i, it is sufficient to sum up the already calculated integrals H_{ij}. However, if H_{ij} are calculated approximately, the question arises as to whether any error is now accumulated in the diagonal element H_{ii}. For the computation of the integrals we use the Gaussian quadrature formula, which allows avoiding computation errors concerned with machine arithmetic [23, pp. 348–354]. Another method, based on a direct calculation of a spatial angle, using its definition and ratios of spherical trigonometry, has been realized in order to check the accuracy of the calculated diagonal coefficients [24]. Comparison of the two described methods of calculating the coefficient H_{ii} shows that the value of the spatial angle, as calculated by the first and the second method, coincide in no less than six significant figures, but the first method is computationally cheaper.

The matrix of the resultant system of linear equations $AQ = B$ is completely filled, asymmetrical and non-sign-determined. During the calculation of test problems, exact methods of solution of the system of linear algebraic equations (the Gaussian method with basic element selection) have been used. Iterative methods (the Gauss-Seidel method, the nonlinear regularity method [25], iteration schemes of incomplete approximation [26] have also been used. The most acceptable of them turns out to be the Gaussian method with major element selection and with the following iterative refinement from the IMSL Microsoft Fortran Power Station library.

Having calculated the velocity values $\left(\frac{\partial\varphi}{\partial x_i}, \frac{\partial\varphi}{\partial y_i}, \frac{\partial\varphi}{\partial z_i}\right), i = \overline{1, N}$, in the mesh nodes being the vertices of plane triangular elements, we can find the new location of the bubble surface and the potential distribution on it. Let us consider the algorithm for the velocity calculation the i-th node. We calculate the velocity components in the local coordinate system for each element, one of the vertices being the i-th node. As tangential directions (j is the element

number) we use the element sides included up to the i-th node. The derivatives for these directions are calculated as the finite differences

$$\frac{\partial\varphi}{\partial s_j}=\frac{\varphi_{m_j}-\varphi_i}{|\bar{s}_j|},\quad \bar{s}_j=(\bar{x}_{m_j}-\bar{x}_i),\quad \frac{\partial\varphi}{\partial\tau_j}=\frac{\varphi_{k_j}-\varphi_i}{|\bar{\tau}_j|},\quad \bar{\tau}_j=(\bar{x}_{k_j}-\bar{x}_i),$$

where m_j, k_j are the numbers of two nodes of the j-th element, the third vertex of which is the i-th node. For the normal direction we use the normal vector $\bar{n}$ averaged over all surrounding elements. The normal velocity is known from the boundary-integral method, that is, $\frac{\partial\varphi}{\partial n_i}=q_i$. The calculated vector $\left(\frac{\partial\varphi}{\partial n_i}, \frac{\partial\varphi}{\partial s_i}, \frac{\partial\varphi}{\partial\tau_i}\right)$ is rearranged for the Cartesian-coordinates vector $\left(\frac{\partial\varphi}{\partial x_i}, \frac{\partial\varphi}{\partial y_i}, \frac{\partial\varphi}{\partial z_i}\right)$. We take as a result the average of the velocity vector for the surrounding elements. Introduction of the weight coefficients as the inverse values of the distances between the surrounding element centers [5] does not result in a more accurate calculation of the velocity.

In the present work we do not use any smoothing algorithms, neither for the bubble surface, nor for the potential values on it, although in some cases numerical instability of the bubble surface and early failure of the calculation occur; smoothing would probably allow such calculations to proceed. Rejection of the use of smoothing algorithms is motivated, first of all, by the fact that using them would result in distortion of the energy characteristics [27] and lead to violation of energy conservation, which in this case is given by [6]

$$3\int_\Gamma \varphi\frac{\partial\varphi}{\partial n}\mathrm{d}\Gamma + V\left(1-\frac{\beta}{1-\lambda}\left(\frac{V_0}{V(t)}\right)^\lambda\right)+\alpha r_z^c = E, \tag{8}$$

where r_z^c is the geometrical bubble center and E the full energy.

In order to demonstrate the performance of the boundary-element method during one time step, we have used the problem of the motion of an absolutely solid sphere in an unbounded fluid domain [28, pp. 152–154]. To demonstrate the numerical algorithm as a whole, and the method of selecting the time step in particular, we have used the Rayleigh problem concerning the collapse of a spherically symmetric bubble. We have also made a comparison with calculations of the axisymmetric problem [29].

4. Computational results

4.1. Bubble oscillations

Let us consider the process of oscillations of a gas bubble in an unbounded fluid domain. In the case under consideration we study a model of a cavitation bubble and assume that the bubble is so small that the influence of gravity can be disregarded. At the initial moment of time the bubble is a sphere of radius $1R_m$ that maintains its spherical shape and is compressed down to the minimum radius under the influence of the hydrostatic pressure. The initial gas pressure, although small, increases with decreasing bubble volume, thereby resisting the moving boundary; bubble collapse is followed by its expansion and vice versa; the bubble evolution becomes oscillatory. In this case the motion of the bubble boundary is described by the Rayleigh equation

$$\xi\ddot{\xi}+\frac{3}{2}\dot{\xi}^2-\beta\xi^{3\lambda}+1=0.$$

where $\xi=R/R_m$ is the non-dimensional radius of the bubble, $\dot{\xi}, \ddot{\xi}$ are the non-dimensional velocity and acceleration of the bubble boundary, respectively. Khoroshev (see [7]) has derived

an approximate dependence of the minimum radius on the gas content parameter β (for $\beta > 0{\cdot}3$)

$$\xi_{\min} \approx \frac{3\beta}{1+3\beta-\beta^{3/2}},$$

where $\xi_{\min}$ is the minimum non-dimensional radius of the bubble, using a numerical integration, taking $\lambda = 4/3$ for simplification. Since this model does not take account of energy losses, the bubble oscillations can last indefinitely. We can traverse only a few oscillations during the numerical simulation, whereupon the numerics fail because of the development of numerical instabilities on the boundary. Figure 3 provides dependencies of the bubble radius on time as obtained from a numerical simulation of the bubble-oscillation process for different values of β (from 0·4 to 0·9); the surface mesh used for this calculation consists of 642 nodes and 1280 elements. It is significant that the bubble keeps its spherical shape for practically the entire duration of the numerical calculation; deviation from spherical symmetry occurs fairly rapidly, causing the calculation to fail. Bubble shapes at the initial moment and the moments of minimum and maximum volumes and also directly before calculation failure are presented in Figure 4 for the case $\beta = 0{\cdot}4$. In all the cases, except for $\beta = 0{\cdot}6$, the development of instabilities takes place during the bubble-growth phase. For β increasing, the bubble oscillation amplitude visibly decreases, and we can expect more oscillations before the moment of calculation failure. Calculations of oscillations with small amplitude are in better agreement with analytical estimates of the minimum radius; variations from the analytically obtained radius minima are 1·25% for $\beta = 0{\cdot}4$ and 0·06% for $\beta = 0{\cdot}9$, respectively, during the first oscillation, and 1·5% and 0·1% during the second oscillation. In all cases the total energy variance before visible development of numerical instability does not exceed 1%. The energy conservation for the case $\beta = 0{\cdot}4$ is shown in Figure 5.

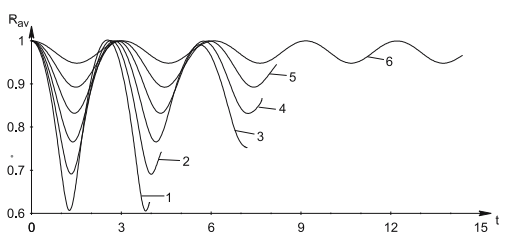

Figure 3. Graphs showing the dependence of the gas-bubble radius on time for different values of $\beta: 1-\beta = 0{\cdot}4, 2-\beta = 0{\cdot}5, 3-\beta = 0{\cdot}6, 4-\beta = 0{\cdot}7, 5-\beta = 0{\cdot}8, 6-\beta = 0{\cdot}9$.

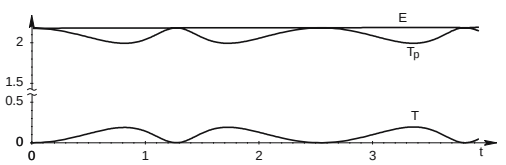

Figure 5. Energy conservation for bubble oscillation ($\beta = 0{\cdot}4$), T – kinetic energy, T_p – potential energy, E – full energy.

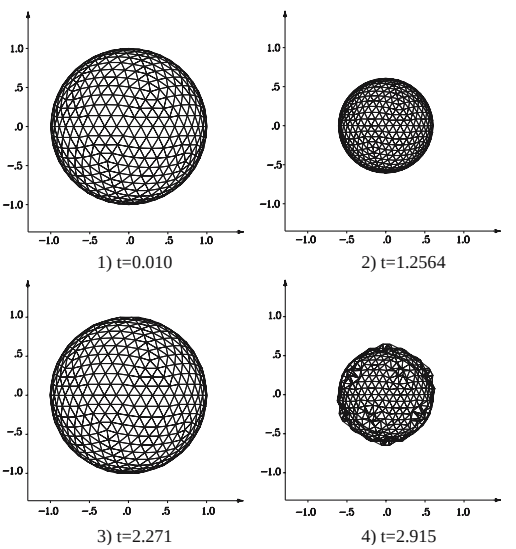

Figure 4. Initial bubble shapes and those at the moments of its minimum and maximum volume and directly before failure of the calculation for the case $\beta = 0{\cdot}4$.

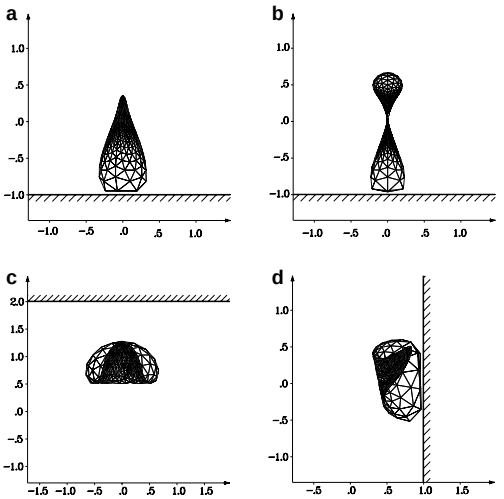

Figure 6. Final phases of bubble evolution for the following cases a) $\varepsilon = \pi, d = 1R_m, \alpha = 0{\cdot}1, \beta = 100$, the second type mesh $N = 642, M = 1280$; b) $\varepsilon = \pi, d = 1R_m, \alpha = 0{\cdot}125, \beta = 100$, the first type mesh $N = 786, M = 1568$; c) $\varepsilon = 0, d = 2R_m, \alpha = 0.2, \beta = 100$, the first type mesh $N = 786, M = 1568$; d) $\varepsilon = \pi/2, d = 1R_m, \alpha = 0{\cdot}2, \beta = 100$, the second type mesh $N = 642, M = 1280$.

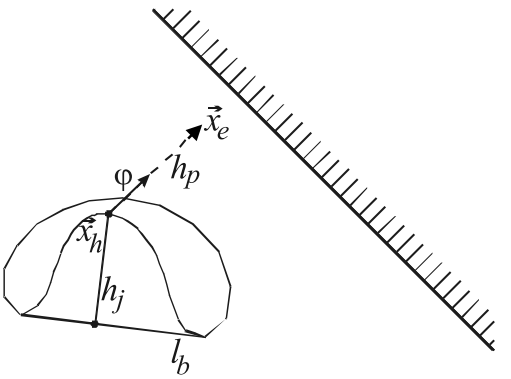

Figure 7. Calculation of the jet penetration coefficient.

Pozrikidis [17] describes the generalized vortex method applied for modelling small and average bubble oscillations. The method allows modelling long periods of bubble existence for minor deformation by taking into account surface tension. The method described here allows modelling the bubble evolution for large deformations; besides, it is possible to model small-amplitude oscillations for long periods of the bubble's existence.

4.2. Evolution of a bubble near a solid wall

Let us consider bubble evolution near a plane solid wall in the presence of gravity. In this case the combined influence of the solid wall and the buoyancy force on the bubble-evolution process creates far more complicated flow structures. For all the calculations described hereafter, the bubble represents a sphere with an initial radius of $R_0 = 0{\cdot}1R_m$; the initial approximation of the potential is taken from the Rayleigh equation for the motion of a gas bubble. The bubble's evolution near a solid wall is under consideration, the buoyancy parameter values being in the range from 0 to 0·2 for different inclinations of the solid wall, *viz.* $\epsilon = 0, \pi/4, \pi/2, 3\pi/4, \pi$, and for the initial distance between the bubble center and the wall running from $1R_m$ to $6R_m$; for the latter the wall influence is practically imperceptible. The most interesting cases are when the bubble is located sufficiently close to the wall: $1R_m - 3R_m$. The bubble, as a rule, remains approximately spherical during the expansion phase. During the collapse phase, in some cases, formation of sharp edges or vertices occurs, causing the calculation to fail (Figure 6a). Besides, the tendency for the bubble dividing into two smaller bubbles has been observed in some cases (Figure 6b). In most cases, during the collapse phase a high-speed jet emanates from the bubble side farthest from the solid wall (Figure 6c, d). The jet penetrates into the bubble toward the solid wall and is deflected by gravity. The jet evolves

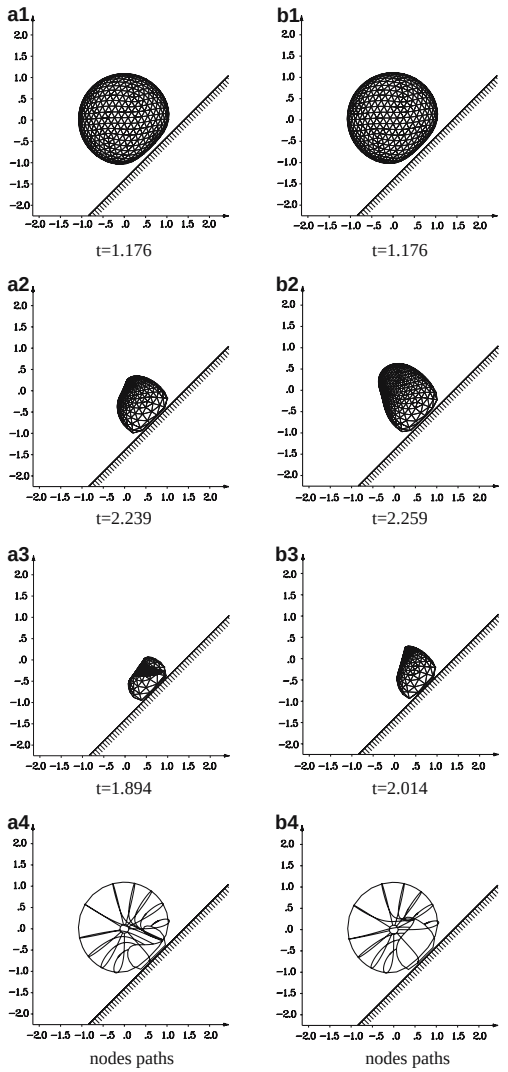

Figure 8. Shapes of the bubble during the collapse phase and tracks of particles for bubble evolution near a solid wall ($d = 1{\cdot}0R_m, \epsilon = 3\pi/4$) for different values of the buoyancy parameter (a) $\alpha = 0{\cdot}025$, b) $\alpha = 0{\cdot}05$) and a second-kind mesh with $N = 642, M = 1280$.

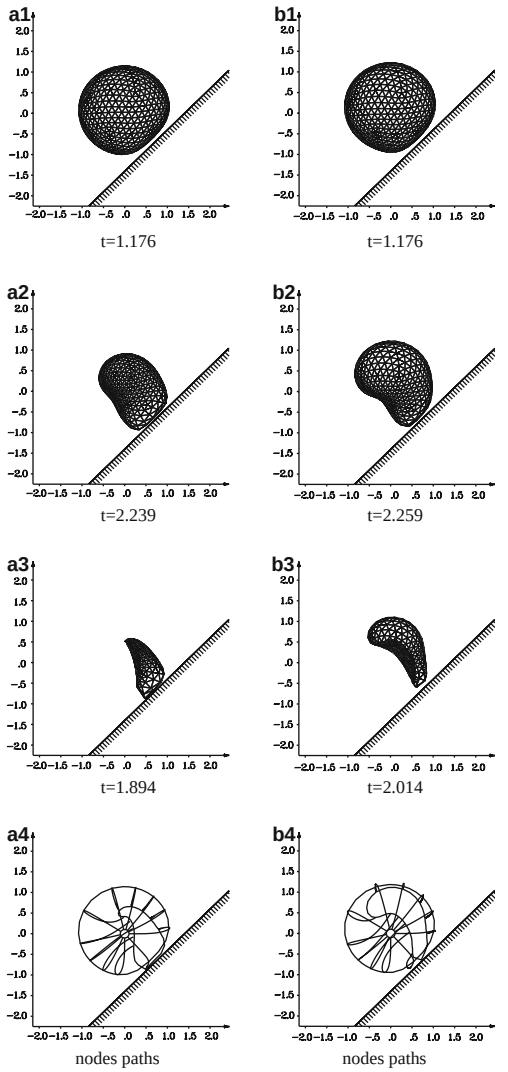

Figure 9. Shapes of the bubble on collapse and particles paths for bubble evolution near a solid wall ($d = 1{\cdot}0R_m, \epsilon = 3\pi/4$) for different values of the buoyancy parameter (a) $\alpha = 0{\cdot}1$, b) $\alpha = 0{\cdot}2$) and a second-kind mesh with $N = 642, M = 1280$.

up to the moment of contact with the opposite surface of the bubble, except for the complex modes when early failure of the calculation occurs.

The most interesting aspect of the three-dimensional model investigation is the direction of the high-speed jet during the bubble collapse phase. Best [30] and Kucera [3] use the Kelvin impulse to predict the direction of jet evolution. This aspect has been studied by us as well, and our findings agree with the conclusions of the above-mentioned authors: when the bubble is located close enough to the solid wall, predictions from Kelvin impulses are often flawed [31]. The aim of this work is to obtain a series of jet characteristics, and dimensional quantities for different types of bubbles, pertaining to cavitation resulting from explosions of different charges.

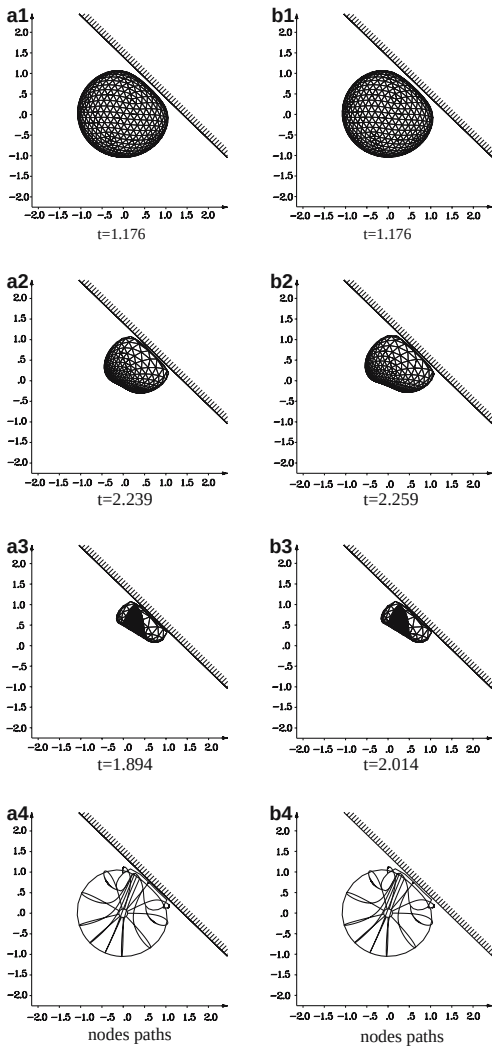

Figure 10. Shapes of bubble during collapse and particles paths for bubble evolution near a solid wall ($d = 1{\cdot}0R_m, \epsilon = \pi/4$) for different values of the buoyancy parameter (a) $\alpha = 0{\cdot}025$, b) $\alpha = 0{\cdot}05$) and a second-kind mesh with $N = 642, M = 1280$.

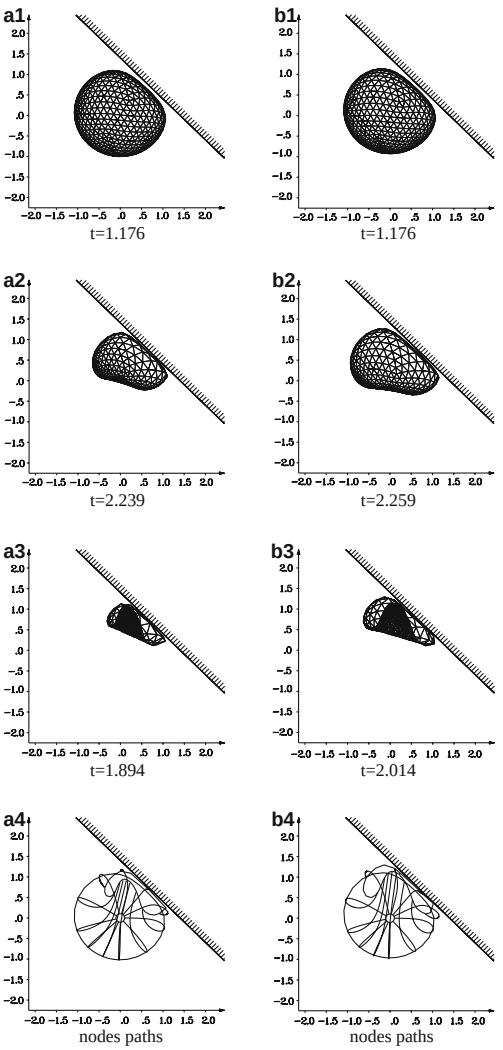

Figure 11. Shapes of the bubble during collapse phase and particles paths for bubble evolution near a solid wall ($d = 1{\cdot}0R_m, \epsilon = \pi/4$) for different values of the buoyancy parameter (a) $\alpha = 0{\cdot}1$, b) $\alpha = 0{\cdot}2$) and a second-kind mesh with $N = 642, M = 1280$.

4.2.1. *Coefficient of jet penetration*

The important factors for estimating the jet's erosive effect are the direction of the jet development, its length and its peak velocity. The depth of penetration of the cumulative jet into the target (in our case the target is a solid wall) L_p and the jet length L_j, the fluid density ρ_i and the density of the target material ρ_m are related by the ratio $L_p = \sqrt{\rho_i/\rho_m} L_j$ [1].

Hence, in the absence of the solid wall, when $\sqrt{\rho_i/\rho_m} = 1$, the jet impacts only for its length without any appreciable velocity loss. That is why we should take into consideration the presence of the fluid layer between the bubble and the solid wall. We draw the vector $(x_l - x_h)$, the origin of which is the jet peak x_h, in the direction of the vector of the peak velocity with the length equal to the jet height $L_j = |x_l - x_h|$ (Figure 7). Having determined

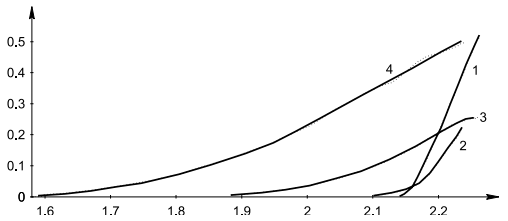

Figure 12. Graphs of the jet height as a function of time for bubble evolution near a solid wall ($d = 1{\cdot}0R_m, \epsilon = 3\pi/4$) for different values of the buoyancy parameter: 1-$\alpha = 0{\cdot}025$, 2-0·05, 3-0·1, 4-0·2).

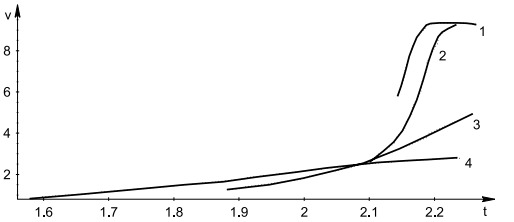

Figure 13. Graphs of the velocity as a function of time for bubble evolution near a solid wall ($d = 1{\cdot}0R_m, \epsilon = 3\pi/4$) for different values of the buoyancy parameter: 1-$\alpha = 0{\cdot}025$, 2-0·05, 3-0·1, 4-0·2).

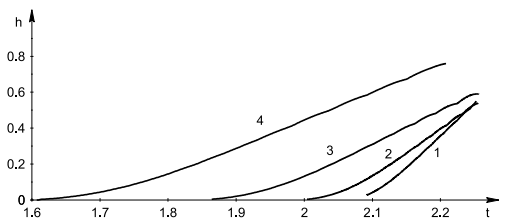

Figure 14. Graphs of the jet height as a function of time for bubble evolution near a solid wall ($d = 1{\cdot}0R_m, \epsilon = \pi/4$) for different values of the buoyancy parameter: 1-$\alpha = 0{\cdot}025$, 2-0·05, 3-0·1, 4-0·2).

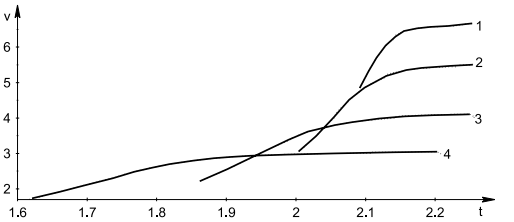

Figure 15. Graphs of the velocity as a function of time for bubble evolution near a solid wall ($d = 1{\cdot}0R_m, \epsilon = 3\pi/4$) for different values of the buoyancy parameter: 1-$\alpha = 0{\cdot}025$, 2-0·05, 3-0·1, 4-0·2.

the dimensionless coefficient of its penetration into the target J_p ($(0 \le J_p \le 1)$, we obtain the adjusted ratio $L_p = \sqrt{\rho_i/\rho_m}\, J_p L_j$. It should be realized that the jet can not hit the target until it attains a sufficiently large velocity. Hence, for a nonnegative coefficient and enough velocity, the jet hits the solid wall.

4.2.2. *Evolution of a bubble near inclined walls*

Let us consider, as an example, two positions of the wall for a minimum distance of the bubble center from the wall $d = 1R_m$. We have succeeded in obtaining nonzero values of the coefficient of penetration for these cases. The first case is a bubble evolving above the inclined wall $\epsilon = 3\pi/4$. Here, for all buoyancy parameter values, a jet is formed which penetrates into the bubble at the collapse phase. Figures 8, 9 provide bubble shapes for different moments of time and values of the buoyancy parameter. For a minimal buoyancy parameter value of $\alpha = 0{\cdot}025$ a sharp jet is formed which is directed toward the solid wall and slightly deflected by gravity. The angle of the velocity gradient with the normal to the wall is 23·4°. In this case the jet has the largest velocity for the given position of the wall, namely $9{\cdot}28\sqrt{\Delta p/\rho}$; the jet length is $0{\cdot}56R_m$ and the coefficient of jet penetration is 0·35. At $\alpha = 0{\cdot}2$ we get a very wide jet, the direction of its evolution making an angle 93·6° with the normal to the solid wall; this jet has the lowest velocity for the given position of the wall. In Figures 12 and 13 graphs giving dependences of the jet height and its velocity on time are shown.

When the bubble evolves under an inclined wall defined by $\epsilon = \pi/4$, the flow structures for different values of the buoyancy parameter vary insignificantly. The impact jets that are formed when the bubble collapses, have a large enough height; thus, for $\alpha = 0{\cdot}2$, the jet height is $0{\cdot}72R_m$ (Figures 10, 11). In this case we have positive coefficients of the jet penetration

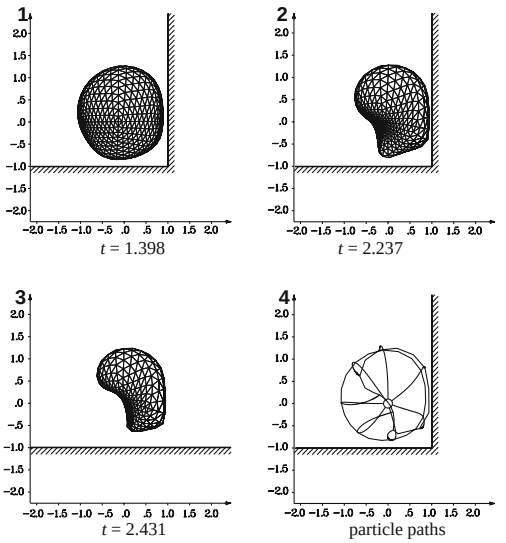

Figure 16. Evolution of the bubble near the angle formed by two solid walls $\alpha = 0{\cdot}2$, $\beta = 100$ and a first-kind mesh with $N = 786$, $M = 1568$.

in the range from 0·94 ($\alpha = 0{\cdot}025$) to 0·71 ($\alpha = 0{\cdot}1$), but now the jet velocities are essentially smaller than in all of the cases described above. For these cases graphs showing the dependences of the jet height and its velocity on time are given in Figures 14 and 15.

Figure 16 presents examples of bubble evolution for acute ($\pi/4$) and obtuse ($3\pi/4$) angles, formed by the solid walls, $\alpha = 0{\cdot}2$, $\beta = 100$.

On the basis of the provided series of calculations it is evident that, during the evolution of a gas-vapor bubble in the vicinity of a plane solid wall ($d = 1R_m$), in most cases a jet of fluid is formed during the collapse phase which penetrates into the bubble. The present model does not allow us to continue the calculations when the simple connectedness of the domain and the boundary intersections is violated. The problem of transforming a 3d-bubble into a torus is partly discussed in [5]. Table 1 gives dimensionless values of the jet height, the coefficient of jet penetration, the angle between the gradient of the velocity field and the outward (with respect to the fluid) normal to the solid wall used in the calculations, when an impact jet is formed when the bubble collapses. For the minimum distance between the bubble and the wall, $d = 1R_m$, the cumulative effect develops most distinctly; the bubble is located close enough to the solid wall and the fluid layer between the bubble and the wall and is minimal. Nonzero coefficients of the jet penetration can be obtained only for this distance between the bubble and the wall. The maximum height of the jet is found for the case $\epsilon = \pi/4, \alpha = 0{\cdot}2$ as $0{\cdot}72R_m$; for this case we also obtain the largest length of the jet penetration $J_p L_j = 0{\cdot}58R_m$. The maximum value of the jet velocity, attained for $\alpha = 0{\cdot}05$, equals $163{\cdot}6\sqrt{\Delta p/\rho}$. We have found the maximum values of the jet peak velocity for two cavitation bubbles and two underwater explosions. We considered cavitation bubbles with maximum radius of 1·27 and 10 mm, as described in [32, Chapter 4]; bubbles were formed during the emission of detonation products in case of an underwater explosion. We considered a bubble formed during the explosion of an underwater mine [28, pp.152–154] and a bubble with a maximum radius of 115 m, formed during the explosion of the "Wigwam" nuclear weapon with a power of 30 Kt [33]. The calculations show that the velocity of the impact jet is always finite, the maximum velocity of the jet is $16{\cdot}26\sqrt{\Delta p/\rho}$ and, as is evident from the provided graphs of the jet velocities (Figures 13, 15), on reaching a certain value, the velocity does not increases further; in

Table 1. Nondimensional characteristics of the bubble and the jet for bubble evolution near solid walls at a distance $d = 1R_m$, for different angles of the wall angle and buoyancy parameter values.

ϵ	α	H	Jp	θ
π	0·025	0·64	0·96	0
	0·05	0·52	0·49	0
$3\pi/4$	0·025	0·56	0·62	23·4
	0·05	0·22	–	48·6
	0·1	0·25	–	76·5
	0·2	0·39	–	93·6
$\pi/2$	0·025	0·55	0·67	25·2
	0·05	0·36	–	42·3
	0·1	0·41	–	58·5
	0·2	0·62	–	70·2
$\pi/4$	0·025	0·61	0·94	15·3
	0·05	0·56	0·81	23·4
	0·1	0·59	0·71	32·4
	0·2	0·72	0·79	37·8
0	0·025	0·54	0·86	0
	0·05	0·54	0·86	0
	0·1	0·56	0·81	0
	0·2	0·64	0·84	0

such cases the velocity graph forms a "shelf", except when numerical failure occurs during the early stages of jet impact long before it contacts the opposite bubble surface. This feature of the jet's behavior was revealed during an investigation of the axisymmetric model of a bubble; this is described in detail in [3]. The maximum velocity of the jet of a cavitation bubble does not exceed 200 m/s. In that way the assumption is proved true once more, namely that the jet of a single cavitation bubble is not able to cause damage to the wall. During explosion of a mine, the maximum velocity of the jet is 205·4 m/s. During a nuclear explosion, the velocity of the jet peak is of the order of the sound speed in water, although not exceeding it, and runs up to 1086·7 m/s. The bubble evolution time for different kinds of bubbles varies essentially. Thus, for cavitation bubbles of the first kind, the lifetime is in the range from 0·00021 to 0·00023 s, for cavitation bubbles of the second kind this is $0{\cdot}00167 - 0{\cdot}00182$ s, for a bubble formed during the explosion of a mine it is $0{\cdot}4 - 0{\cdot}445$ s and for the explosion of a nuclear weapon it is $3{\cdot}61 - 4$ s.

5. Conclusion

This paper has been devoted to the investigation of the dynamics of a single gas-vapor bubble. The fluid is assumed to be inviscid and incompressible and the flow is irrotational. As an instrument of numerical investigation we have used a boundary-element method on the basis of the third Green formula. Two methods of building surface meshes are employed. For the calculation of the regular and singular integral coefficients we have used the same approach: the inner integrals are calculated analytically, upon which we use a 7-point Gaussian quadrature to calculate the external integrals. For the solution of the resultant system of linear equations we have used the Gaussian method with consequent iterative refinement. The conservative

character of the numerical algorithm can be traced by constantly checking the conservation of total energy. Using the described numerical method we have realized the numerical simulation of bubble oscillations in an unbounded fluid domain, disregarding the influence of gravity. Since this model does not yield any energy losses, theoretically such oscillations should last infinitely long. The numerical model is not completely comparable with the analytical one since it introduces numerical viscosity. In the process of numerical simulation we have managed to obtain from two to five incomplete oscillations, depending on the value of the gas-content parameter. The minimum bubble radii found during numerical simulation are in accordance with the analytical estimates. Failure of the numerical calculation occurs as a result of the arising numerical instability of the bubble surface. Besides, we have considered bubble evolution near plane inclined solid walls. The main aim of this work has been to investigate such characteristics of the jet as its height, velocity, and direction of evolution. The introduced coefficient of jet penetration allows refining the ratio given in [1]. The positive coefficients of penetration were obtained for the minimum distance between the bubble and the wall, $d = 1R_m$. We have also derived dimensional characteristics for cavitation bubbles and bubbles formed as a result of the explosion of a mine or a nuclear weapon.

In the future we intend to apply this method with a higher-order approximation of the functions on the elements. The higher-order approximation will probably allow making the calculation more stable. Besides, application of a linear approximation does not allow taking into consideration the influence of surface tension. This is an additional argument in favor of the higher-order approximation.

The disadvantage of the boundary-element method applied for this class of problems is the impossibility of calculating the collapsing bubble transforming into a torus without using any additional implicit approaches. In this respect, methods which allow one to easily turn from a simply connected domain geometry to a multi-connected one are more favorable. See, for instance, the method described in [15].

Acknowledgements

The authors wish to thank M. M. Afanasieva, A. M. Goudov and especially A. G. Terentiev for their contribution to the present work. We would like to thank an anonymous referee whose constructive comments have contributed to a substantially improved final manuscript.

References

1. V. K. Kedrinskij, *Explosion Hydrodynamics. Experiment and Models*. Novosibirsk: Publishing House of the Siberian Branch of RAS (2000) 435 pp. (in Russian)
2. A. A. Korobkin, Asymptotic theory of liquid-solid impact. *Phil. Trans. R. Soc. London* A335 (1997) 507–522.
3. J. P. Best and A. Kucera, A numerical investigation of non-spherical rebounding bubbles. *J. Fluid Mech.* 245 (1992) 137–154.
4. T. B. Benjamin and A. T. Ellis, The collapse of cavitation bubbles and the pressures thereby produced against solid wall. *Phil. Trans. R. Soc. Lond.* A260 (1966) 221–240.
5. Q. X. Wang, The evolution of a gas bubble near an inclined wall. *Theoret. Comput. Fluid Dyn.* 12 (1998) 29–51.
6. O. V. Voinov and V. V. Voinov, On the scheme of a cavitation bubble collapse near a wall and the impact jet formation. *Papers of the AS USSR* N1 227 (1976) 63–66 (in Russian).
7. Y. L. Levkovskij, *Structure of Cavitation Streams.* Leningrad: Sudostroenie (1978) 222 pp. (in Russian).
8. J. R. Blake, J. M. Bouton-Stone and R. P. Tong, Boundary integral methods for rising, bursting and collapsing bubbles. In: H. Power (ed.), *BE Applications in Fluid Mechanics. Mechanics Publications, Southampton* (1995) pp. 31–71.

9. Q. X. Wang, E. K. Png and B. H. Tan, Numerical simulation of evolution three-dimensional bubbles. In: E. P. Rood (ed.), *Proc. 22nd Symposium on Naval Hydrodynamics*. Washington, Aug 9–14 (1998) pp. 282–300.
10. Q. X. Wang, Numerical simulation of violent bubble motion. *Phys. Fluids* 16 (2004) 1610–1619.
11. J. P. Best, The rebound of toroidal bubbles. In: J. R. Blake, J. M. Boulton-Stone and N. H. Thomas (eds.), *Bubble Dynamics and Enterface Phenomena*, Dordrecht: Kluwer Acad. Publ. (1994) pp. 405–412.
12. J. R. Blake, Y. Tomita and R. P. Tong, The art, craft and science of modelling jet impact in a collapsing cavitational bubble. *Appl. Sci. Res.* 58 (1998) pp. 77–90.
13. J. C. W. Rogers, W. G. Szymczak, Computations of violent surface motions: Comparisons with theory and experiment. *Phil. Trans. R. Soc. London* A 355 (1997) 649–663.
14. M. Sussman and P. Smereka, Axisymmetric free boundary problems. *J. Fluid Mech.* 341 (1997) 269–294.
15. N. J. Lawson, M. Rudman, A. Guerra and J.-L. Lions, Experimental and numerical comparisons of the break up of a large bubble. *Experiments in Fluids*, Heidelberg: Springer-Verlag 26 (1999) 524–534.
16. C. W. M. Van der Geld, On the motion of a spherical bubble deforming near a plane wall. *J. Engng. Math.* 42 (2002) 91–118.
17. C. Pozrikidis, Numerical simulation of three-dimensional bubble oscillations by a generalized vortex method. *Theoret. Comput. Fluid Dyn.* 16 (2002) 151–169.
18. A. M. Goudov and M. M. Afanasieva, Modeling of spatial problems of the ideal fluid by the boundary element method. In: A. G. Terentiev (ed.), *High Speed Hydrodynamics: Inter-University Collection of Scientific Works*, The Chuvash State University, Cheboksari (1990) pp. 15–24 (in Russian).
19. K. E. Afanasiev and A. M. Goudov, Numerical modeling of dynamics of a spatial bubble by the boundary element metrhod. *Modeling in Mechanics* (Novosibirsk) 7(24) No1 (1993) 11–19. (in Russian).
20. A. G. Terentiev, K. E. Afanasiev and M. M. Afanasieva, Simulation of unsteady free surface flow problems by the direct boundary element method. In: Th. A. Cruse (ed.), *Advanced Boundary Element Method*, IUTAM Symposium. Heidelberg: Springer-Verlag (1988) pp. 427–434.
21. G. Chahine, R. Duraswami and M. Rebut, Analytical and numerical study of large large bubble/bubble and bubble/flow interaction. 19th ONR Symp. of Naval Hydrodynamics, Seoul (1992) pp. 125–144.
22. F. Ghassemi, Automatic mesh generation scheme. *Computing and Structures* 15 (1982) 613–626.
23. K. I. Babenko, *Principles of Numerical Analysis*. Moscow: Nauka (1986) 744 pp. (in Russian).
24. I. V. Grigorieva, Peculiarities of numerical solution of spatial problems on dynamics of the incompressible fluid by the boundary element method. In: V. P. Zhitnikov (ed.), *Proceedings of the International scientific conference 'Modelling, Calculations, Designing in Conditions of Indetermination - 2000'*, Ufa, Russia (2000) pp. 176–180 (in Russian)
25. V. N. Trushnikov, One nonlinear regulating algorithm and some of its applications. *J. Higher Math. Phys.* 19 (1979) 822–829 (in Russian).
26. K. E. Afanasiev, A. M. Goudov and Yu. N. Zakharov, The use of iteration schemes of incomplete approximation in some problems of hydrodynamics. *Modelling, Measurement & Control*, B, AMSE Press. 46(4) (1992) 27–40.
27. K. E. Afanasiev and T. I. Samoilova, Technique of using the boundary element method in problems with free boundaries. *Computing Technologies*, Novosibirsk 11(7) (1995) 19–37 (in Russian).
28. H. Lamb, *Hydrodynamics*. Moscow, Leningrad: OGIZ, State Publ. House (1947) 928 pp.
29. K. E. Afanasiev and I. V. Grigorieva, The investigation of bouyant gas bubble dinamics near an inclined wall. In: G.G. Cherny *et al.* (eds), *HSH-2002 International Summer Scientific School. High Speed Hydrodynamics. Proceedings*, Cheboksary, Russia (2002) pp. 111–119.
30. J. P. Best, The Kelvin impulse: application to cavitation bubble dynamics. *J. Aust. Math. Soc. Ser.* B30 (1988) 127–146.
31. J. R. Blake, B. B. Taib and G. Doherty, Transient cavities near boundaries. Part 1. Rigid boundary. *J. Fluid Mech.* 170 (1986) 31–71.
32. R. Knepp, J. Daily and F. Hammit, *Cavitation*. Moscow: Mir (1974) 687 pp. (in Russian).
33. J. W. Pritchett, Incompressible calculations of underwater explosion phenomena. In: V. N. Nikolaevskij (ed.), *Proc. Second Internat. Conf. on Numerical Methods in Fluid Dynamics*. Berlin: Springer (1971) pp. 422–428.